Applied Catalysis B: Environmental 292 (2021) 120142

Contents lists available at ScienceDirect

Applied Catalysis B: Environmental

journal homepage: www.elsevier.com/locate/apcatb

Exceptional performance of gold supported on fluoridated hydroxyapatite catalysts in CO-cleanup of H_2-rich stream: High activity and resistance under PEMFC operation conditions

Zouhair Boukha *, Juan R. González-Velasco, Miguel A. Gutiérrez-Ortiz

Chemical Technologies for Environmental Sustainability Group, Department of Chemical Engineering, Faculty of Science and Technology, University of the Basque Country UPV/EHU, P.O. Box 644, E-48080, Bilbao, Spain

ARTICLE INFO

Keywords:
Gold catalyst
Hydroxyapatite
Hydroxyfluorapatite
Fluorapatite
CO preferential oxidation
PEMFC

ABSTRACT

Proton-exchange-membrane fuel cells (PEMFCs) appear to be the most promising solution for future automotive applications. Facing the lack of efficient hydrogen storage and transportation solutions, current research is focused on the development of on-board catalytic reformers. In this strategy, the purity of hydrogen stream is still an unresolved issue that needs to be addressed in order to avoid poisoning of the Pt electrodes of PEMFC.

Here we report the extraordinary performance of gold supported on fluorine-substituted hydroxyapatite (HAP) catalysts in the CO preferential oxidation (COPROX) process. At 80 °C, the optimized catalyst (Au/F-(1)) proves to be highly active, selective (showing a CO conversion (X_{CO}) of 100 % and selectivity towards CO_2 production (S_{CO2}) close to 62 %) and very resistant to deactivation, even in the presence of H_2O (15 %) and CO_2 (20 %). In addition, these results were obtained at relatively high weight hourly space velocity (WHSV: 60,000 $cm^3\ g^{-1}\ h^{-1}$). It should be highlighted that our catalysts clearly outperform state-of-the-art gold catalysts. Our discovery introduces Au/F(x)-HAP catalysts as a viable solution for an effective elimination of CO to feed PEMFCs with CO-free hydrogen streams.

1. Introduction

Hydrogen fuel cells present one of the best strategies for replacing power generation systems. Among them, PEMFC has attracted an increasing interest because it offers a large power density and a high efficiency to transform hydrogen into energy (60 %) compared with that achieved by traditional combustion processes (33–35 %) [1]. Moreover, its low operating temperatures (60−80 °C) allow working with a good response to a variable energy demand. These properties make PEMFC the most suitable type for automotive applications. However, since hydrogen is mostly produced by hydrocarbons or alcohols reforming processes, it has been necessary to develop a variant of the process to satisfy its purity requirements. For this purpose, the Water-Gas Shift (WGS) reaction is widely used as a first purification stage, allowing the reduction of the CO content to a value close to 1%. Further, by means of COPROX reaction acceptable concentrations could be achieved to feed the fuel cell. Thus, COPROX catalysts meant for PEMFC applications should be capable to reduce CO concentration from 1% to below 50 ppm and to maintain acceptable selectivity to CO_2 (S_{CO2}, at least 50 %) at 80 °C, under complex mixtures, including CO, CO_2, O_2, H_2 and H_2O [2–5]. For instance, realistic methanol steam reformate contains up to 25 % CO_2 and 10−15% water [4].

It is known that nano-sized gold catalysts exhibit a good catalytic performance in COPROX at low temperatures (≤ 120 °C). Many reports associated their superiority with their high specific activity for CO oxidation and their low capacity to dissociate hydrogen [6,7]. However, there are issues that limit their application which mainly consist of (i) the negative effect of the presence of CO_2 and/or H_2O and (ii) their low resistance to deactivation during a long-term operation. In this scenario, various formulations have been investigated in order to approximate the operation conditions of Au catalysts to those required by PEMFCs. A special attention has been paid to reducible supports and/or promoters (such as CeO_2, Fe_2O_3, MnO_x and Cu). In this sense, it has been proved that the presence of oxygen vacancies facilitates electron transfer from the support to the surface gold particles leading to the formation of negatively charged $Au^{\delta-}$ species [6,8,9]. The latter significantly lowers the hydrogen conversion, which promotes COPROX activity. Besides, many reports pointed out that COPROX activity of gold catalysts can be

* Corresponding author.
E-mail address: zouhair.boukha@ehu.eus (Z. Boukha).

https://doi.org/10.1016/j.apcatb.2021.120142
Received 19 January 2021; Received in revised form 7 March 2021; Accepted 11 March 2021
Available online 17 March 2021

improved through the use of alkali metals or alkali earth metals as promoters [3,13] and/or the addition of a second active transition metal [10].

Nevertheless, very few gold catalysts demonstrated a reasonable efficiency and a long-term stability under simulated reformate gas atmospheres [3,5,12–14]. In fact, only Landon et al. [2,11] had reported an excellent behavior over a 5%Au/Fe_2O_3 catalyst, in the presence of 50 % H_2, 4.7 % H_2O and 22 % CO_2 (showing a CO conversion of 99.5 % and selectivity close to 51 % at 80 °C). They stressed that it was essential to achieve a complete reduction of residual cationic gold during the pre-treatment of the catalyst in order to prevent the occurrence of the reverse WGS reaction which decreases CO conversion. Unlike the latter finding, all available studies dealing with different gold catalyst formulations showed that neither high activity nor acceptable selectivity was achieved, under realistic COPROX conditions. For instance, Qiao et al. [12] found that CeO_2-supported Au single atoms were highly active and selective in COPROX over a wide temperature window (50−100 °C). However, their stability test at 80 °C showed that the CO conversion decreased from 94 % to 84 % in the initial 20 h. Moreover, the addition of 10 % H_2O and 20 % CO_2 to the reaction mixture provoked a profound decay of their activity which did not exceed 10 % at 80 °C. Laguna et al. [5] studied the effect of the presence of CO_2 and H_2O in the COPROX feed-stream on the activity of an AuCeCu catalyst. Though it proved to be water-tolerant, its activity decreased as the CO_2 concentration in the feed-stream increased. They attributed this behavior to a competitive adsorption of CO_2 over the CO oxidation active sites. Lin et al. [3] studied the performance of an Au/La-Al_2O_3 catalyst under PEMFC operation conditions. They found that with La addition the window for maximal CO conversion shifted to higher temperatures and expanded from 30−70 °C to 50−100 °C. The observed improvement was explained by the formation of $LaAlO_3$ phase which suppressed H_2 oxidation and favored CO adsorption on Au sites. However, due to carbonate accumulation, their catalyst suffered a gradual deactivation (from 80 to 63 %) during 20 h time-on-stream (TOS), in the presence of high concentration of CO_2 (20 %). Lakshmanan et al. [14] observed a significant improvement of COPROX activity over Au/MO_x/Al_2O_3 (M = La, Ce, and Mg) catalysts compared with a free-promoter sample (Au/Al_2O_3). Moreover, among all tested catalysts, the lanthana-modified one exhibited the best catalytic performance. They attributed the superiority of the latter to a lower oxidation-state of Au species. Nevertheless, the synthesized formulation resulted not suitable for demanding conditions; since the addition of 10 % H_2O to the feed decreased the maximum CO conversion from 99 to 86 % and shifted it from 63 to 115 °C.

In the last few decades, the application of HAP ($Ca_{10}(PO_4)_6(OH)_2$) material as a catalyst support has attracted considerable attention. The presence of phosphate and hydroxyl groups seems to provide stabilization and a synergistic effect with a variety of active phases which explain its promising results in numerous applications [15–24]. Moreover, owing to its structural flexibility the HAP lattice presents a high ion-exchange capacity which allows a tuning of its surface chemistry and then its reactivity. For instance, fluoride ions (F^-) can easily replace hydroxyl group sites to form the fluorapatite (FAP, $Ca_{10}(PO_4)_6F_2$). In our previous study on HAP and FAP supports, we showed that a complete fluoridation of HAP incremented the density of surface acid centers [22]. In parallel, the loss in the surface hydroxyl coverage significantly lowers the number of the basic sites. Due to this surface chemistry modification, the FAP support resulted more efficient for both the dehydration and dehydrogenation activity (using 2-butanol oxidation as a probe reaction).

In this study, we present for the first time the properties and behavior of gold supported on fluorine-substituted HAP catalysts in COPROX reaction. To the best of our knowledge, the potential of our system in COPROX has not been previously studied.

2. Experimental

2.1. Preparation of the catalysts

Five apatite supports presenting different amounts of fluorine (0−4 wt.%) were synthesized by co-precipitation method, using Ca$(NO_3)_2{\cdot}4H_2O$, $(NH_4)_2HPO_4$ and NH_4F salts. The precipitate was redissolved in a nitric acid solution then neutralized with ammonia at a pH 10. After filtration, the recovered solid was washed with purified water and then dried at 120 °C for 12 h. Finally, the samples were calcined in air at 500 °C for 4 h. The resulting supports will be hereafter referred to as F-(x); where "x" represents the nominal F content (wt.%). The range of F concentrations (0−4 wt.%) was selected in order to obtain a free-fluorine HAP sample (namely F-(0)), samples containing both fluoride and hydroxyl ions (Hydroxyfluorapatite, $Ca_{10}(PO_4)_6(O-H_yF_z)$, namely F-(1), F-(2) and F-(3), respectively) and FAP (namely F-(4)), respectively.

Then, Au/F-(x) catalysts were prepared by deposition-precipitation with urea (DPU); starting from $HAuCl_4$ (Aldrich) as a precursor. The support (7 g) was suspended in a solution (210 mL) containing a concentration of 2.54 $mmol_{Au}$ L^{-1}. After the addition of 5.3 g of urea (Panreac) the suspension was heated to 80 °C under stirring for 20 h. The pH of the suspension was maintained around 8.5. Finally, the samples were filtered, washed and dried at 100 °C for 12 h. The activation of the prepared catalysts consisted of their reduction at 400 °C (5 °C min^{-1}) under a 20 % H_2/He flow for 2 h.

2.2. Characterization techniques

The contents of Ca, P and Au were determined by means of inductively coupled plasma atomic emission spectroscopy (ICP-AES); whereas the actual concentration of fluorine was determined by wavelength dispersive X-ray fluorescence (WDXRF).

The textural properties of the activated catalysts were investigated by N_2 physisorption experiments at -196 °C on a Micromeritics (TRISTAR II 3020) apparatus. Before their analysis, the samples were evacuated at 300 °C under nitrogen flow for 8 h.

The powder XRD analyses were conducted on a X'PERT-MPD X-ray diffractometer with Cu Kα radiation.

The XPS surface analyses were performed with a SPECS apparatus equipped with Phoibos 150 1D-DLD analyzer and monochromatic Al Kα radiation. The conductivity of the samples was enhanced using an electron flood gun. To correct the charging effects, the C 1s binding energy (BE) was used as a reference.

Fourier transform infrared (FTIR) spectra for the reduced Au/F-(x) samples diluted in KBr were recorded on a CARRY 600 apparatus. The spectra covering the range 4000−400 cm^{-1} were obtained by accumulation of 54 scans and a resolution of 4 cm^{-1}.

The size and the dispersion of Au particles for the reduced Au/F-(x) samples were investigated by transmission electron microscopy (TEM). The observations were performed on a Philips CM200 microscope using a LaB6 filament and working at 200 kV. On the other hand, the maps showing the Ca, P, F and Au distributions were collected combining high-angle annular dark field (HAADF) micrographs with X-EDS analyses. In these studies, we used a FEI Titan Cubed G2 60–300 microscope at 300 kV equipped with a Schottky X-FEG field emission electron gun, a monochromator, CEOS GmbH spherical aberration (Cs) corrector and a Super-X EDX system under HAADF detector for Z contrast imaging in STEM conditions. The EDX microanalysis was realized using a probe current of 240 pA and a semi-convergence angle of 10 mrad. HAADF STEM images were also taken using an inner detector radius of 63.5 mrad.

FTIR spectroscopy was also used for the CO adsorption studies. The self-supported samples were introduced in a high temperature cell equipped with ZnSe windows (Specac). Prior to the adsorption, the samples were pre-treated at 400 °C, for 30 min, under 20 %H_2/N_2 flow

(200 cm^3 min^{-1}) and purged with N_2 flow for 1 h. After a subsequent cooling to 30 °C under N_2 (30 min), the background spectrum was recorded averaging 52 scans with a resolution of 4 cm^{-1}. Then, 30 spectra were recorded (one spectrum per minute) after exposure to 750 ppm CO (diluted in N_2) at 30 °C (during 30 min). The evolution of the catalysts under CO oxidation reaction conditions has also been investigated at 30 °C. In this case, the reduced samples were exposed to 750 ppm CO and 3% O_2 (diluted in N_2) for 30 min.

The H_2, CO, CO_2, NH_3 and H_2O chemisorption studies, respectively, were carried out using a Micromeritics AutoChem 2920 instrument coupled to a mass spectrometer (Hiden Analytical). The samples were pretreated under 5% H_2/Ar flow (50 cm^3 min^{-1}) at 400 °C for 90 min. After cooling to 80 °C, a series of pulses (loop volume: 0.5 cm^3) were injected in He carrier (50 cm^3 min^{-1}) until saturation of the catalyst surface.

The oxygen storage capacity complete (OSCC) and oxygen storage capacity (OSC) experiments were carried out at 80 °C on the same experimental setup used for the chemisorption studies. The reduced catalysts were pre-treated in a flow 5%H_2/Ar at 400 °C (30 min) followed by a treatment with He (30 min) at the same temperature. For the OSCC measurements, the samples were submitted to an oxidative treatment with a 5% O_2/He flow (50 cm^3 min^{-1}) for 30 min, followed by evacuation under He for 15 min. Afterwards, the samples were reduced under a 5% CO/He flow (50 cm^3 min^{-1}). The OSCC values were determined by integration of the peak of CO_2, produced during the treatment with 5% CO/He. After purging with He (for 20 min), the OSC measurements were performed on the same samples. The latter were submitted to six alternating series of pulses (CO-O_2) where the OSC was determined as the average amount of the formed CO_2 for each CO pulse.

2.3. Catalytic performance testing

The catalytic tests were performed in a tubular flow reactor (ID 9 mm) operating at atmospheric pressure. The standard tests were carried out using 100 mg of the catalyst (160−250 μm) diluted with quartz (to achieve a bed volume of 1.5 cm^3) and a total flow of 100 cm^3 min^{-1}; which corresponds to a WHSV of 60,000 cm^3 g^{-1} h^{-1}. Before their testing, the reduced catalysts were pretreated under the reaction mixture at 120 °C for 2 h. The light-off experiments were sequentially carried out by increasing the reaction temperature from 40 to 120 °C. CO conversion and selectivity were recorded after 40 min at each reaction temperature. Three different feed gas mixtures were used in each investigated reaction as follows:

- 1% CO and 1% O_2 in CO total oxidation (COTOX) reaction (40−120 °C).
- 1% CO, 1% O_2 and 50 % H_2 in a model COPROX reaction (40−120 °C).
- 1% CO, 1% O_2, 50 % H_2, 20 % CO_2 and 15 % H_2O in a realistic COPROX reaction (60−120 °C).

In order to examine the stability of the catalysts, additional experiments were carried out under the realistic COPROX conditions at 80 °C for a prolonged TOS (up to 70 h). Before their testing, the reduced catalysts were heated in He flow (100 cm^3 min^{-1}) at 80 °C. Over the optimized catalysts, the experiments were performed at least two times, where reproducible results were obtained.

The specific activity and activation energy values (using 10−15 mg of catalyst) were determined under COTOX conditions. For these calculations, low CO conversion values (< 15 %) were considered, in order to ensure differential reactor conditions. The experiments for the estimation of the specific activity in COPROX reaction were performed under a mixture composed of 2% CO, 0.4 % O_2 and 40 % H_2 (balanced with He). These conditions were selected in order to maximize the selectivity towards CO_2 production. H_2 oxidation reaction rate was also determined under a mixture composed of 1% O_2 and 3% H_2 (balanced with He).

The water vapor was fed continuously using a GILSON 307 pump. The analysis system consisted of a Gas Chromatograph (Agilent Technologies 490 Micro GC) equipped with a TCD detector. The latter has a detection limit of 10 ppm. CO conversion (X_{CO}), O_2 conversion and selectivity to CO_2 (S_{CO2}) values, respectively, were calculated as follow:

$$X_{CO} = \frac{F_{CO}^{in} - F_{CO}^{out}}{F_{CO}^{in}} \times 100 \quad (1)$$

$$X_{O2} = \frac{F_{O2}^{in} - F_{O2}^{out}}{F_{O2}^{in}} \times 100 \quad (2)$$

$$S_{CO2} = \frac{X_{CO}}{X_{O2}} \times \frac{1}{\lambda} \times 100 \quad (3)$$

where "F_{in}" and "F_{out}" represent the inlet and outlet molar flows of the reactants, respectively, and "λ" represents the oxygen excess, determined as follows:

$$\lambda = 2 \times \frac{F_{O2}^{in}}{F_{CO}^{in}} \quad (4)$$

3. Results and discussion

3.1. Chemical composition and textural properties

Table 1 lists the chemical composition of all reduced Au/F-(x) catalysts. The determined Ca/P molar ratio is slightly higher (1.68–1.73) than that corresponding to a stoichiometric apatite (1.67). Interestingly, the F concentration determined for the Au/F-(4) sample (3.55 %) is very close to that required for a complete incorporation of fluoride ions into the apatite lattice to form a FAP structure (Fig. S1). However, the composition of the Au/F-(1), Au/F-(2) and Au/F-(3) samples appears to be intermediate between hydroxyapatite and fluorapatite forms, presenting a partial replacement of hydroxide for fluoride. According to Fig. S1 the substitution degree is around 29 % for Au/F-(1), 64 % for Au/F-(2) and 86 % for Au/F-(3).

The N_2 physisorption isotherms and the distribution of the pore sizes for all reduced Au/F-(x) catalysts are included as Supplementary material (Figs. S2 and S3, respectively). The shapes of both the isotherms and hysteresis loops observed in all of them are very similar. Moreover, the distributions of the pore sizes reveal that all analyzed samples may be considered as mesoporous materials presenting maxima centered between 15 and 40 nm, Fig. S3. Data obtained from the analysis of the N_2 isotherms are summarized in Table 1. The fluorine-free catalyst (Au/F-(0)) shows a BET specific surface area (S_{BET}) equal to 57 m^2 g^{-1}. The S_{BET} seems to increase with fluorine contents, attains its maximum at 3 wt.% (97 m^2 g^{-1}) and then decreases to 44 m^2 g^{-1} at higher fluoride content (4 wt.%). In parallel, the latter exhibits the largest mean pore size (27.3 nm vs. 11.5 nm in the Au/F-(3) sample). The observed differences in the textural properties of the prepared catalysts can be linked to an evolution in their structural properties induced by their modification with fluorine.

3.2. Structural properties

The structural properties of the prepared samples were investigated by XRD techniques. Fig. 1 displays the patterns of the bare supports and their corresponding Au-modified samples. The diffractograms of the bare supports show that they crystallize in the hexagonal system and belong to $P6_3/m$ group (JCPDS 01 − 082–2956). Unlike Au/F-(3), the rest of the Au/F-(x) samples exhibit an additional peak at 38.2° with a very low intensity, assigned to (111) reticular plane of metallic gold (JCPDS 00-004-0784). The absence of this feature on the Au/F-(3) diffractogram can be explained by the deposition of relatively highly dispersed Au particles.

Table 1
Chemical composition and textural properties of the Au/F-(x) catalysts, reduced at 400 °C.

Sample	ICP			WDXRF		BET		
	Ca/P[a]	Nominal Au wt.%	Actual Au wt.%	F, wt.%	F/Ca[b]	S_{BET}, $m^2\ g^{-1}$	V_p[c], $cm^3\ g^{-1}$	d_p[d], nm
Au/F-(0)	1.73	1.5	1.09	0	0	57	0.31	20.3
Au/F-(1)	1.68	1.5	1.08	1.03	0.06	83	0.40	17.4
Au/F-(2)	1.69	1.5	1.10	2.20	0.13	82	0.36	17.2
Au/F-(3)	1.69	1.5	1.10	3.08	0.17	97	0.34	11.5
Au/F-(4)	1.72	1.5	1.10	3.55	0.20	44	0.30	27.3

[a] Ca/P atomic ratio as determined by ICP.
[b] F/Ca atomic ratio as determined by WDXRF.
[c] Pore volume, as determined by application of BJH method.
[d] Mean pore diameter, as determined by application of BJH method.

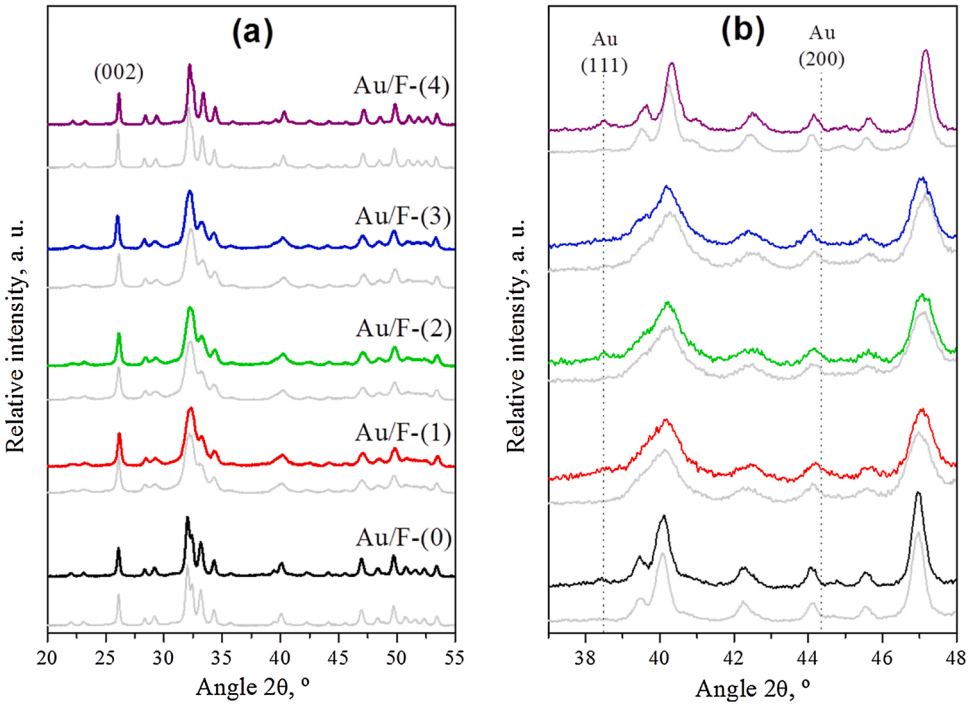

Fig. 1. (a) XRD patterns of the bare supports (lower) and reduced Au/F-(x) catalysts (upper) and (b) their zoom in the 2θ angle range of 37-48°.

The XRD data listed in Table 2 show that the lattice parameter "a" decreases with the progressive incorporation of F, which may be due to the larger radius of hydroxyl group compared with fluoride ion [27,28]. On the other hand, the estimated apatite crystallite size is about 38.9 nm for Au/F-(0) and 46.2 nm for Au/F-(4) sample. However, the partially fluoridated samples ($1 \leq F \leq 3$) show significantly lower values (28.2–28.8 nm); suggesting that they present a lower crystallinity degree [25–27]. These results are in good agreement with the differences observed in the textural properties of the analyzed samples. Rodríguez-Lorenzo et al. [27] observed a similar behavior in their study on the influence of fluorine in the synthesis of apatites. They attributed the presence of smaller Ap crystallites in the partially fluorinated samples to the slowest rate of their crystallization process compared with HAP and FAP. They reported that the apatite structure preferentially incorporates

Table 2
XRD and TEM data for the reduced Au/F-(x) catalysts.

Catalyst	XRD			TEM	
	d_{AP}, nm[a]	a, Å[b]	c, Å[b]	d_{Au}[c], nm	D_{Au}[d], %
Au/F-(0)	38.9	9.4176 (± 0.001)	6.8842 (± 0.0005)	2.8 (± 0.6)	38.6
Au/F-(1)	28.7	9.4157 (± 0.001)	6.8750 (± 0.0006)	3.3 (± 1.6)	27.3
Au/F-(2)	28.2	9.4085 (± 0.001)	6.8789 (± 0.0004)	4.2 (± 2.0)	24.8
Au/F-(3)	28.8	9.4055 (± 0.001)	6.8912 (± 0.0006)	1.9 (± 0.4)	52.0
Au/F-(4)	46.2	9.4032 (± 0.002)	6.8797 (± 0.0004)	2.7 (± 0.7)	38.6

[a] Apatite crystallite size as determined by Scherrer equation, by using the (002) diffraction peak.
[b] Apatite lattice parameters.
[c] Average Au particle size (TEM).
[d] Au dispersion (TEM).

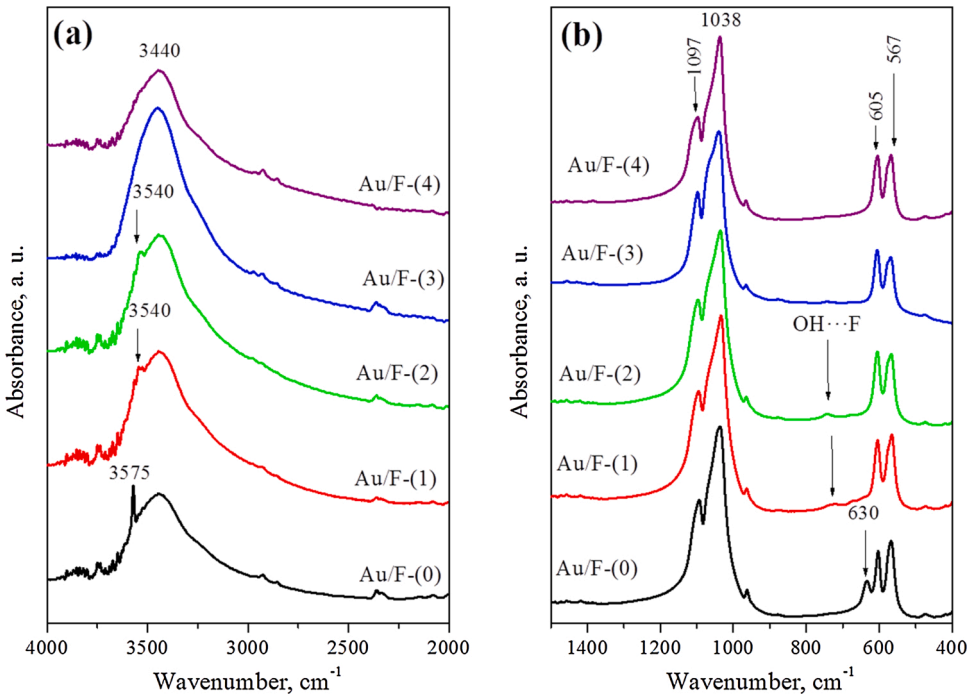

Fig. 2. FTIR spectra of the reduced Au/F-(x) catalysts: (a) 4000-2000 cm^{-1} and (b) 1500-400 cm^{-1} domain.

the F^- ions, but the subsequent insertion of OH groups would require a longer maturation time. This interpretation actually makes sense, considering the small size of the fluoride ion in comparison with the OH groups.

In order to gain further insight into the structural properties, the reduced Au/F-(x) samples have also been analyzed by FTIR spectroscopy. As it can be deduced from Fig. 2, the spectra of all catalysts are analogous to those corresponding to the apatite structures [16–20]. The absorption bands occurring at 567, 605, 1038 and 1097 cm^{-1} are ascribable to different vibration modes of P—O bonds in the $(PO_4)^{3-}$ groups [24]. The spectra also contain a broad band (3000−3750 cm^{-1}) characteristic of adsorbed water. The spectrum of Au/F-(0) shows two small and sharp bands at 3575 and 630 cm^{-1}, assigned to the valence vibrations (ν_S) and the oscillations (ν_L) of hydroxyl groups, respectively [24]. According to You et al. [29], the OH groups on the hydroxyapatite surface are rather crystallographic and serve as binding sites for calcium and phosphate ions. Interestingly, the ν_S band shifts to a lower wavenumber forming a shoulder at 3540 cm^{-1} in the case of Au/F-(1) and Au/F-(2) samples. In parallel, a new band appears near 735 cm^{-1} which can be assigned to F···OH pairs [27]. The latter completely disappears at higher F loadings (> 2 wt.%). This observation, together with the absence of the ν_L band in the F-modified samples spectra, points out that upon increasing the F content the hydroxyl sites are progressively substituted by F- ions in the apatite network [22,23,27].

3.3. XPS surface analysis

The surface composition and the oxidation state of the Au species on the reduced catalysts were investigated using XPS techniques. The results are summarized in Table 3 and Fig. 3, respectively. The surface Ca/P atomic ratio values for all analyzed samples (1.49–1.59) are significantly lower than those given by the ICP analysis (1.65–1.70). This effect is more pronounced in the case of the Au/F-(2) sample which presents the lowest Ca/P value (1.49); suggesting that the Ca species are relatively less exposed on its near surface. As it can be observed in Fig. 3, in the Au 4 $f_{7/2}$ region, the Au/F-(0) sample displays a symmetric peak centred at 83.3 eV, assigned to metallic Au [15]. The progressive addition of F smoothly shifts the position of this feature to lower BE values (up to 82.8 eV for the Au/F-(4) sample). Moreover, FWHM data reported in Table 3 reveal a relatively broader Au 4f7/2 peak (> 2.6 eV) in the case of the partially fluoridated samples ($1 \leq F \leq 3$); indicating a larger heterogeneity in Au environments. In good agreement with FTIR results, this heterogeneity would mainly be attributed to the simultaneous presence of OH^- and F^- species on the catalysts surface.

3.4. Morphology and nano-structural analysis

Fig. 4 includes TEM micrographs of all reduced Au/F-(x) catalysts. It can be observed that the gold particles spread on all samples present a quasi-spherical shape. The estimation of the average Au particle sizes, listed in Table 2, reveals that it is ranging between 1.9 nm, for Au/F-(3), and 4.2 nm, for Au/F-(2). These results point out that the preparation method used for the gold deposition on our series of supports is suitable for obtaining highly dispersed particles (< 5 nm). It should be noted that, the detection of the smallest Au particles on the Au/F-(3) sample is consistent with the absence of the Au characteristic peaks in its XRD

Table 3
XPS data for the reduced Au/F-(x) catalysts.

Catalyst	Au ($4f_{7/2}$), eV	Au ($4f_{5/2}$), eV	FWHM Au ($4f_{7/2}$), eV	F (1 s), eV	O (1 s), eV	Au/P[a]	F/P[a]	Ca/P[a]
Au/F-(0)	83.3	86.9	2.441	–	530.9	0.0194	0	1.54
Au/F-(1)	83.2	86.9	2.687	684.3	530.8	0.0103	0.07	1.53
Au/F-(2)	82.9	86.5	2.668	685.1	531.5	0.0115	0.12	1.49
Au/F-(3)	82.9	86.4	2.693	685.4	531.2	0.0180	0.18	1.52
Au/F-(4)	82.8	86.5	2.236	684.7	531.1	0.0240	0.27	1.59

[a] Atomic ratio.

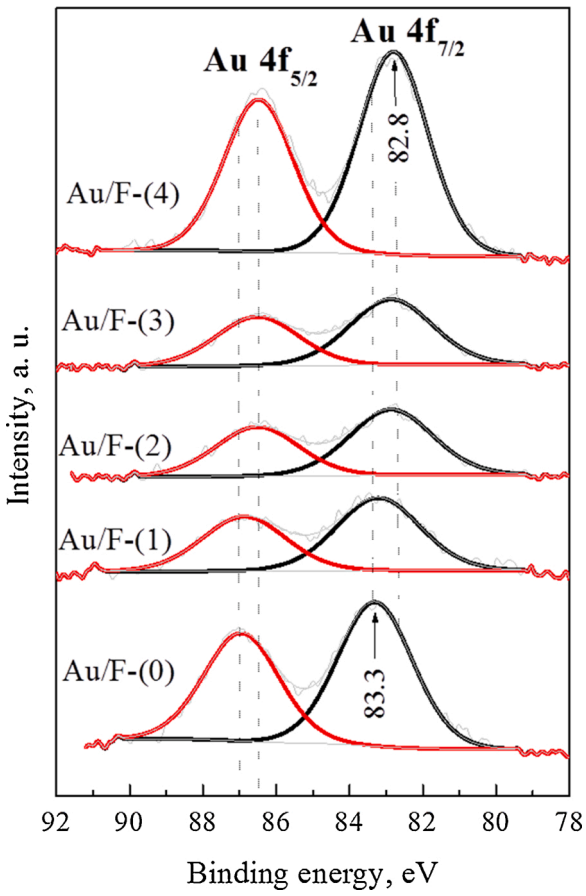

Fig. 3. XPS spectra for the reduced Au/F-(x) catalysts in the Au 4f region.

patterns. Interestingly, the Au/F-(2) sample shows a wider distribution of the Au particle sizes, followed by the Au/F-(1) sample. By contrast, the distributions observed on Au/F-(0), Au/F-(3) and Au/F-(4) samples are relatively narrower, where the measured sizes are generally lower than 5 nm. On the other hand, in good agreement with XRD data, the size of apatite support particles is significantly larger on the Au/F-(0) and Au/F-(4) when compared with the partially fluorinated catalysts. This confirms once again the high degree of crystallinity shown by the former.

In order to gain insight into the elemental distributions with a finer detail, the samples were also analyzed through combining HAADF-STEM and nano-analytical techniques. Fig. 5a displays the HAADF images and the resulting EDX maps corresponding to Au, Ca, P and F elements. The F maps reveal that on all F-modified samples fluorine is homogeneously dispersed. Upon increasing the F content, its observed density increases; but no local concentration could be detected. This general tendency confirms the total incorporation of fluoride ions into the apatite structure. On the other hand, in consistency with TEM results, the Au maps evidence the presence of fine particles and some local concentrations, more pronounced on the Au/F-(1) and Au/F-(2) samples. On the other hand, on the HAADF-STEM images for Au/F-(0), Au/F-(1), Au/F-(2) and Au/F-(4) samples, we can visualize, in agreement with the XRD data, the lattice spacing corresponding to the (111) plane (0.235 nm) of deposited Au crystallites (Figs. 5b, c, S4a and b, respectively).

3.5. Oxygen storage capacity and volumetric chemisorption studies

By means of OSCC the maximum reducibility of the catalysts can be quantified while the OSC provides a quantification of the most reactive and available oxygen atoms. Generally, at the metal-support interface oxygen can be reversibly stored and stabilized by the support [30]. The oxygen atoms are, then, released and migrate onto the metallic surface, where they are available for oxidation.

The OSCC and OSC studies at 80 °C for the reduced Au/F-(x) catalysts are summarized in Fig. 6a. It is worth noting that all bare supports do not display any oxygen storage activity. Thus, it is reasonable to assume that the OSCC activity of the gold-modified catalysts is mainly linked to defects in the Au-supports interface. To facilitate their comparison, the values corresponding to gold catalysts were all referred to 1 m^2 of the BET surface area. As expected, data reported in Fig. 6a show that the OSC values are about one order of magnitude smaller than those corresponding to OSCC. Nevertheless, the evolutions of OSCC and OSC with the fluorine loading are almost identical. For instance, the density of bulk oxygen stored on the F-free catalyst (Au/F-(0)) is about 0.51 $\mu mol_{CO2}\ m^{-2}$. This value seems to decrease with the F content to reach a minimum (0.23 $\mu mol_{CO2}\ m^{-2}$) at 2 wt.% F before increasing up to 0.74 $\mu mol_{CO2}\ m^{-2}$ over the Au/F-(4) catalyst. The observed tendency can be associated with the structural properties of the used support, induced by its modification with fluorine. In this sense, it is found that both OSC and OSCC increase with increasing the support crystallite size (Fig. S5). This suggests that the growth of the support crystallite size promotes both the surface (OSC) and bulk (OSCC) diffusion of oxygen atoms. This is in good agreement with data reported by Ozkan et al. [31] in their study on the impact of particle size of ceria on the oxygen storage capacity. They explained the observed trend by an enhancement of reversible oxidation/reduction at lower degree of structural disorder. In fact, in our case, the highest OSC and OSCC values are obtained on the samples presenting the highest degree of crystallinity (Au/F-(0) and Au/F-(4)) which reflects a lower structural disorder. By contrast, it seems that, due to its low degree of crystallinity, a partial fluoridation of hydroxyapatite hinders oxygen vacancy creation.

On the other hand, the results corresponding to the volumetric chemisorption studies using different probe molecules, performed at 80 °C, are shown in Fig. 6b. As it can be deduced from their analysis, the adsorption capacity for H_2, CO_2 and H_2O, respectively, generally decrease with increasing the F content. This would mainly be related to a loss in the surface basic sites induced by a decrease in the number of the exposed hydroxyl groups. By contrast, the use of NH_3 as a probe molecule reveals that the number of the acid sites is rather higher for the samples presenting a larger specific surface area (196, 184 and 230 $\mu mol_{NH3}\ g^{-1}$ for Au/F-(1), Au/F-(2) and Au/F-(3), respectively). Besides, the measured amounts of chemisorbed CO are in all cases very small to give reliable data on the number of the active Au species (Fig. 6b). The Au/F-(2) sample presents the highest capacity to chemisorb CO (n_{CO}^{chem} = 1.48 $\mu mol_{CO}\ g^{-1}$) followed by the Au/F-(1) sample (0.96 $\mu mol_{CO}\ g^{-1}$). Data reported in Fig. S6 show that there is a clear correlation between the amounts of chemisorbed CO and the average particle size, as determined by TEM, where n_{CO}^{chem} increases with the average size of Au particles. This unexpected tendency could be explained by the modification of the support properties and the nature of the metal-support interface.

3.6. FTIR studies of CO adsorption and CO oxidation reaction

In order to study the nature of CO-Au interactions after activation of the Au/F-(x) catalysts (reduction at 400 °C), an investigation was carried out using CO adsorption monitored by FTIR spectroscopy (Fig. 7a). In consistency with the XPS data, the CO adsorption on all samples gives rise to a strong band located at 2105−2109 cm^{-1} which can be assigned to metallic Au species [32]. This feature easily disappears during N_2 purge (not shown). Moreover, the spectra present additional weak bands, centered between 1975 and 2020 cm^{-1}, attributed to strongly adsorbed CO in a bridge bonded configuration [14,33]. These bands result from an electron transfer from the support to small Au clusters which become negatively charged. Interestingly, a comparison with a

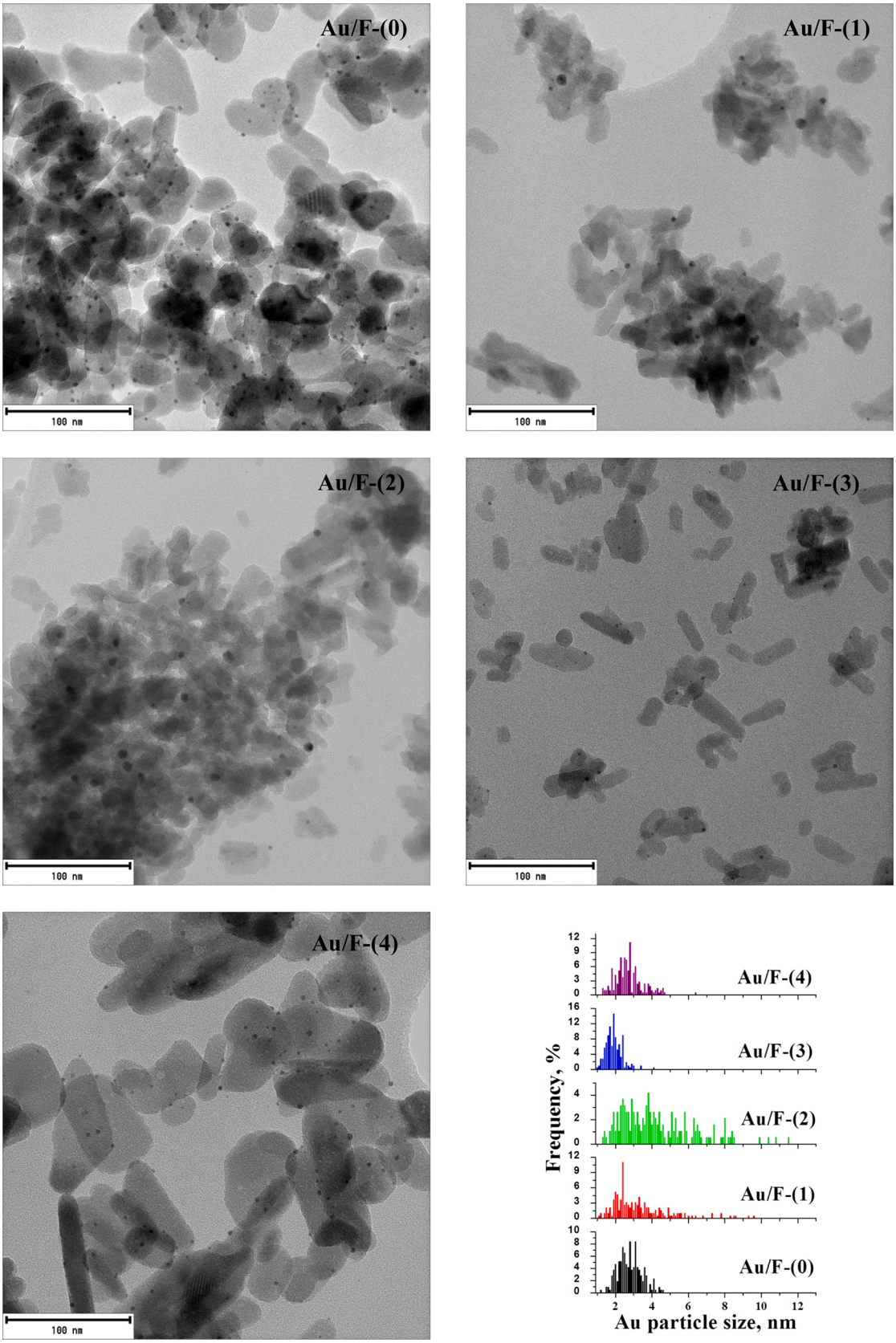

Fig. 4. TEM micrographs and Au particle sizes distribution for the reduced Au/F-(x) samples.

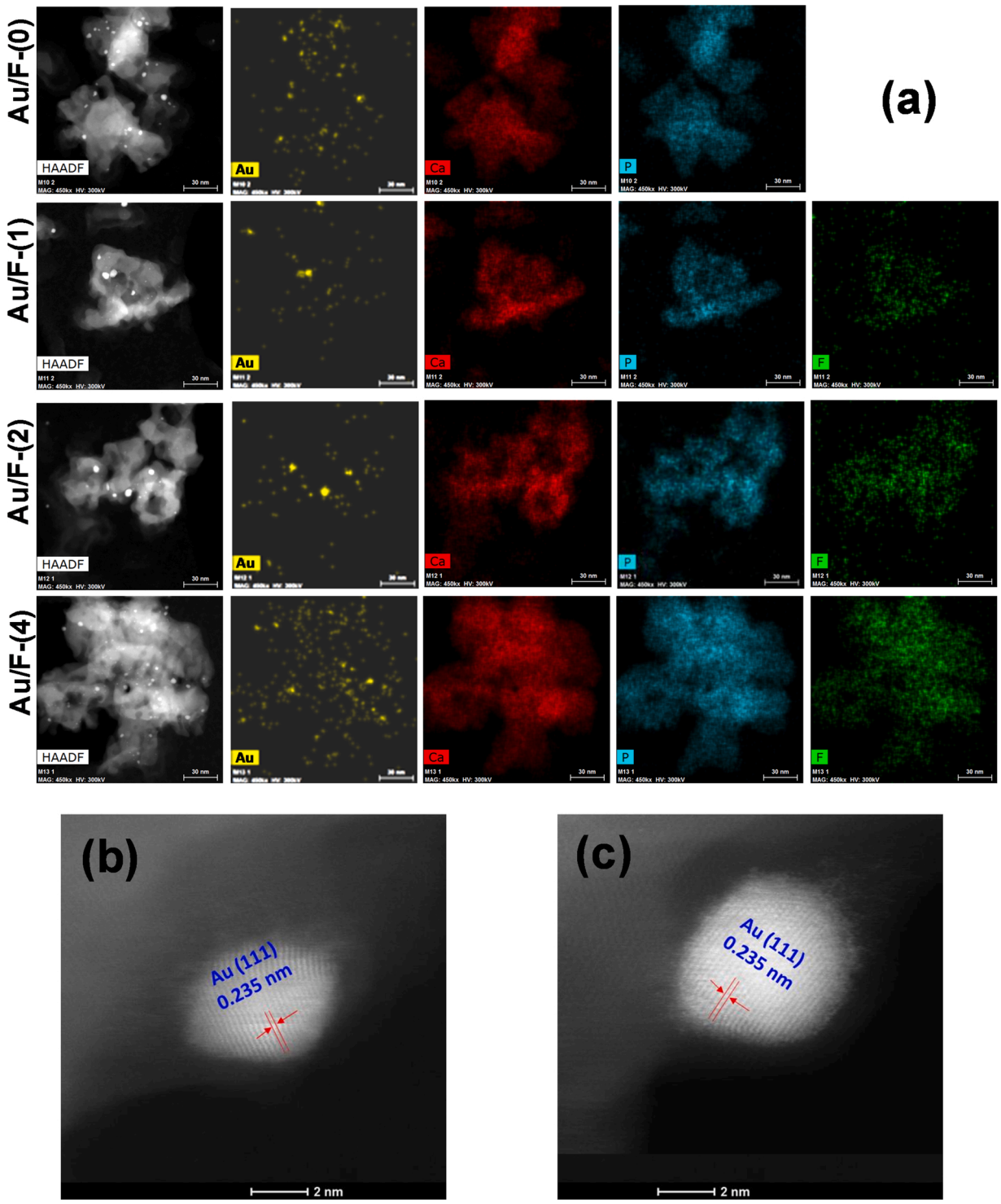

Fig. 5. HAADF study for the reduced Au/F-(x) catalysts. (a) images displaying the colour maps for Au, Ca, P and F given by X-EDS analysis. (b) and (c) represent the HAADF-STEM images coresponding to Au/F-(0) and Au/F-(1) samples, respectively. (For interpretation of the references to colour in this figure, the reader is referred to the web version of this article).

previous study reveals that these features are relatively much less intense than those observed on the spectra of reduced Au/TiO_2 and Au/Fe_2O_3, reported by Boccuzzi et al. [33].

The CO-Au interactions with oxygen inlet have also been investigated at 30 °C (Fig. 7b). With reference to the spectra plotted in Fig. 7a, the spectra corresponding to the CO oxidation reaction (Fig. 7b) show a shift of the main CO adsorption band towards high wavenumbers (2113−2116 cm^{-1}). This displacement can be associated with an evolution in the oxidation state of gold species. In agreement with a number of earlier studies, this feature can be assigned to CO adsorbed on electropositive gold species ($Au^{\delta+}$), induced by adsorbed oxygen [34]. It is worth noting that this band is much broader in the case of the Au/F-(2), tending to split into two bands centred at 2116 and 2136 cm^{-1}, respectively (Fig. S7). This effect would imply the presence of additional adsorption sites more positively charged; probably occurring on the Au-support interface [35]. Interestingly, at a higher F content

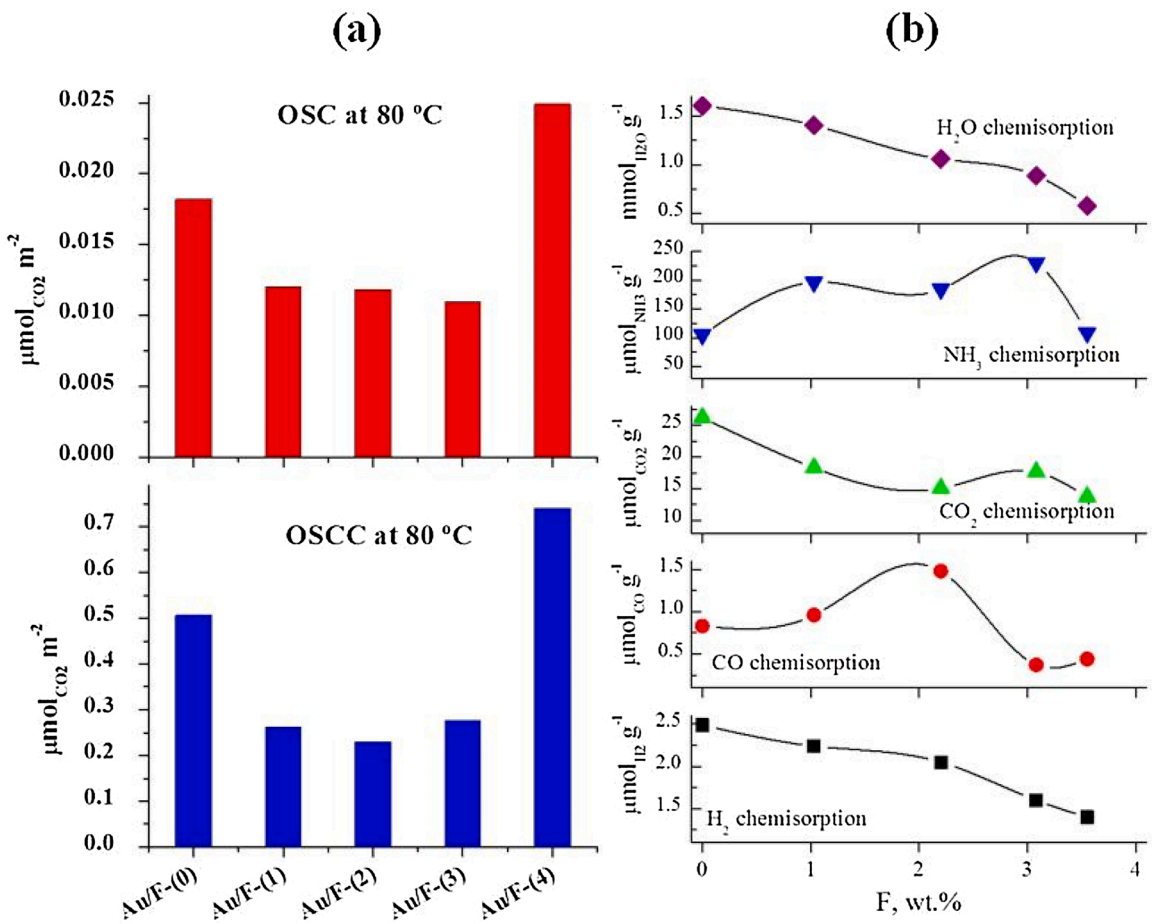

Fig. 6. Evolution of (a) OSC (upper) and OSCC (lower) and (b) H_2, CO, CO_2, NH_3 and H_2O chemisorption capacity as a function of F content, measured at 80 °C.

(Au/F-(3)) the latter shift to higher wavenumbers (from 2136 to 2177 cm^{-1}) and seems to resists N_2 purge (Fig. S8). A similar feature was observed by Venkov et al. [35] on the spectra recorded on an Au/Al_2O_3 system. They attributed its presence to the adsorption of CO on Au^+ species. Furthermore, a significant difference may be noticed in the nature of CO_2 species detected in the range 2300−2400 cm^{-1}. While the Au/F-(0), Au/F-(1) and Au/F-(4) samples present a doublet characteristic of $CO_{2gas\ phase}$, the Au/F-(2) and Au/F-(3) samples give rise to a strong band peaked at 2350 cm^{-1} due to CO_2 adsorbed on oxidized gold species [36]. In parallel, a significant loss in the intensity of the CO adsorption bands can be observed; suggesting that produced CO_2 is probably adsorbed on the same type of active site as that of CO [37]. These results evidence the effect of the support on the electronic properties of Au particles and the nature of the adsorption sites involved in the CO oxidation reaction. In turn, these differences point out that the CO oxidation reaction proceeds via distinct mechanism pathways.

A special attention was also paid to the evolution of the characteristic regions of adsorbed water molecules (2700−3720 cm^{-1}) and carbonates species (1280−1740 cm^{-1}), respectively, under CO oxidation mixtures (Fig. S9). All spectra show a broad band in the 2750−3750 cm^{-1} region due to the adsorbed water molecules [16]. The accumulation of these adsorbed forms seems to be much slower on the Au/F-(2) and Au/F-(3) samples. Moreover, bands ascribable to adsorbed carbonate species (1240−1665 cm^{-1}) can be observed on all gold catalysts together with an effective dehydroxylation of their surface; where surface hydroxyl bands give rise to negative signals in the range 3720−3667 cm^{-1} and those centered between 3536 and 3570 cm^{-1} (detailed presentation in Fig. S10). Regardless of the proposed mechanism it is often assumed that hydroxyl group plays an important role in the activation of CO oxidation reaction [7,43,47]. For instance, a reaction between adsorbed CO and surface hydroxyl species was proposed to generate carboxyl (COOH) intermediates which decompose to form CO_2 [7,47].

3.7. Catalytic activity

3.7.1. Catalytic performance in the COTOX reaction

Fig. 8a displays the COTOX light-off curves over the reduced Au/F-(x) catalysts. With the reactor filled up with fluorine-free catalyst, the CO conversion is around 37 % at 40 °C and it increases with the reaction temperature to reach 88 % at 80 °C and 100 % at 110 °C. The addition of 1 wt.% F does not significantly affect the CO conversion values. However, at higher F loadings a slight improvement in the activity can be observed, where the Au/F-(3) sample shows the highest CO conversion values. Fig. 8b reports the specific activity data for all studied catalysts, as determined under differential reactor conditions. Note that the values estimated at 80 °C are in the range of those reported previously over Au/Al_2O_3 and $Au/La\text{-}Al_2O_3$ catalysts (0.48–1.95 $mmol_{CO}\ g_{Au}^{-1}\ s^{-1}$) [3]. Irrespective of the reaction temperature, the partially fluorinated catalyst (Au/F-(3)) is the most active one followed by the Au/F-(2) catalyst. For instance, at 80 °C the specific activity of Au/F-(3), 1.36 $mmol_{CO}\ g_{Au}^{-1}\ s^{-1}$, is 2.2 times higher than that of the fluorine-free catalyst (0.6 $mmol_{CO}\ g_{Au}^{-1}\ s^{-1}$). Thus, it can be concluded that the efficiency of the studied catalysts in COTOX does not depend on their redox properties, since the catalyst presenting the lowest OSC value exhibits the highest specific activity. Instead, the notable improved textural properties together with the substitution of large amounts of crystallographic hydroxyl groups by fluoride ions in the former make it advantageously more active. By contrast, a high surface hydroxyl coverage seems to penalize the activity of gold particles spread on the Au/F-(0) and Au/F-(1) surface.

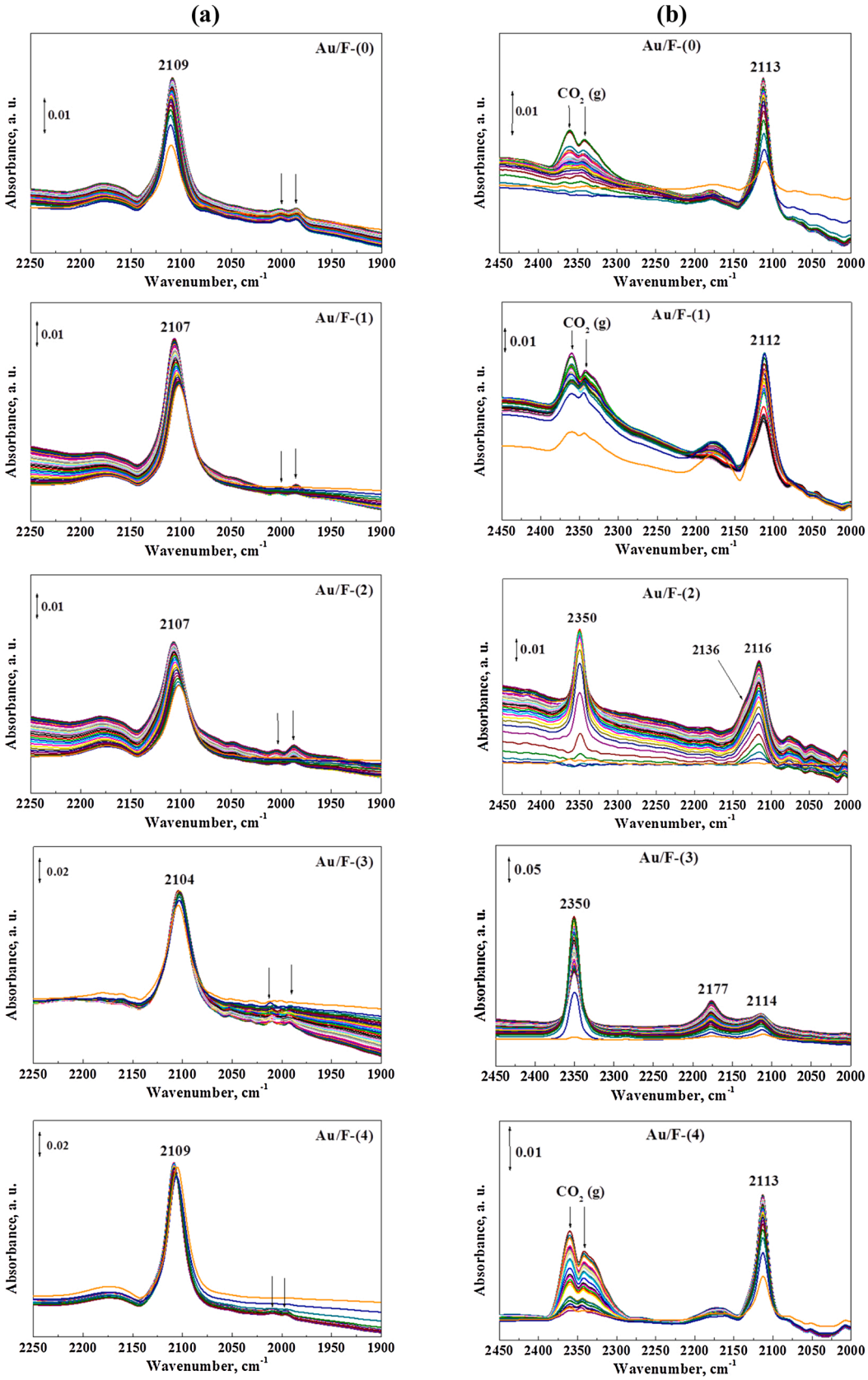

Fig. 7. FTIR spectra for the reduced Au/F-(x) catalysts recorded for 30 min after exposure to (a) CO adsorption (750 ppm) and (b) CO + O_2 mixture (750 ppm and 3%, respectively).

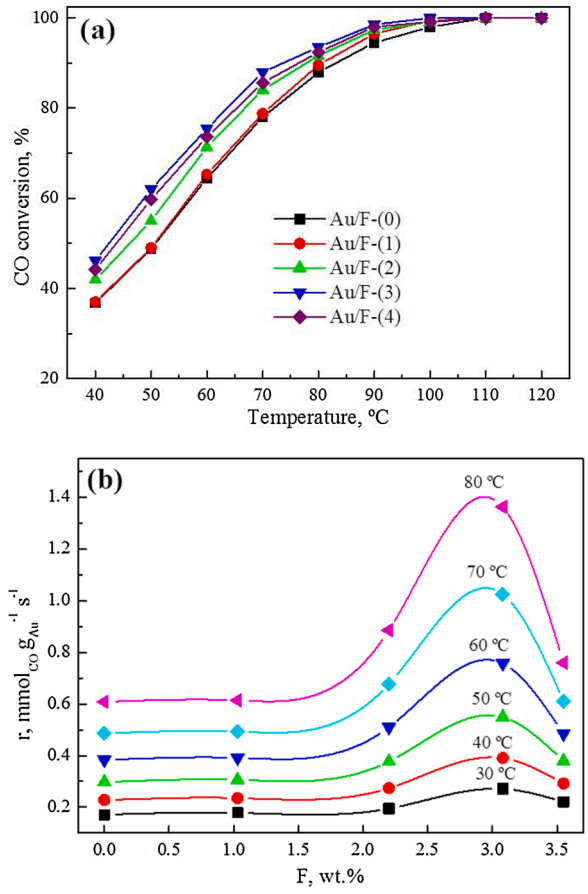

Fig. 8. Catalytic activity of the reduced Au/F-(x) catalysts in COTOX reaction (1% CO and 1% O_2 balanced with He): (a) Light-off curves (WHSV = 60,000 $cm^3\ g^{-1}$) and (b) Variation of the specific activity with F content, estimated under differential reactor conditions.

Table 4 lists the apparent activation energy (Ea) data extracted from Arrhenius plots in the 30–80 °C temperature range (Fig. S11). The analysis of the Ea values estimated over our Au/F-(x) catalysts (22–28.6 kJ mol^{-1}) reveals that they are close to those reported previously over Au/CeO_2 [38], Au/Al_2O_3 [39], Au/TiO_2 [40], Au/Fe_2O_3 [41] and Au/HAP [42]. It is worth noting that the Ea for Au/F-(2) (26.9 kJ mol^{-1}) and Au/F-(3) (26.9 kJ mol^{-1}) are significantly higher than those estimated over the rest of the catalysts (22–22.5 kJ mol^{-1}). In line with the FTIR results, this difference can be associated with a difference in the mechanism of the CO oxidation reaction, which proceeds through distinct pathways. As stated before, over Au/F-(2) and Au/F-(3), after being generated, CO_2 molecules are adsorbed on the catalyst surface. By contrast, on the Au/F-(0), Au/F-(1) and Au/F-(4) catalysts, larger amounts of adsorbed CO and gas phase CO_2 are detected, suggesting that the produced CO_2 is readily evacuated.

3.7.2. Catalytic performance in the COPROX reaction

Fig. 9a and a' display the performance of Au/F-(x) catalysts in COPROX reaction in terms of CO conversion and selectivity, respectively. The light-off curves of the fluorine-free catalyst (Au/F-(0)) show its maximal CO conversion (84 %) at 70 °C; which corresponds to a S_{CO2} value close to 44 % (Fig. 9a and a', respectively). Upon increasing the reaction temperature both the CO oxidation activity and selectivity gradually decrease. According to the literature data, this behavior can be associated with the competitive H_2 and CO oxidation reactions, involving the same activated oxygen species [5,43,44]. The addition of 1% F markedly improves the activity and selectivity and lowers the temperature of the maximum CO conversion (93 %) to 60 °C. The position of T_{max} is maintained for all fluorinated samples, but the overall activity seems to depend on the F loading, where at T < 70 °C it follows this general trend: Au/F-(3) > Au/F-(2) > Au/F-(1) > Au/F-(4) > Au/F-(0). At higher temperatures, the decrease in X_{CO} and S_{CO2} values seems to be much slower using high F loadings (Au/F-(3) and Au/F-(4)).

A comparison of the behavior of the catalysts in COTOX and COPROX reveals a significant improvement of their activity in the presence of hydrogen at T ≤ 70 °C. This promoting effect of H_2on the CO oxidation activity was reported in previous studies [21,43,44]. Quinet et al. [44] associated this effect to the stabilization of −OOH species which react with CO to form CO_2. This interpretation is in line with the high COPROX reaction rate (2.45–4.2 $mmol_{CO}\ g_{Au}^{-1}\ s^{-1}$) compared with that estimated for the COTOX reaction (0.6–1.36 $mmol_{CO}\ g_{Au}^{-1}\ s^{-1}$) (Table 4).

Feeding water (15 %) and CO_2 (20 %) markedly affects the shape of the activity and selectivity curves (Fig. 9b and b', respectively). Over all assayed samples, the temperatures corresponding to the maximal X_{CO} shift to higher values and a significant increase in the selectivity can be observed. As in the case of the ideal COPROX mixture, the fluorine-free catalyst shows the lowest efficiency; where its maximal CO conversion, centered at 80 °C, does not exceed 84 %. However, over the F-modified catalysts the maximal CO conversion approaches 100 % and its temperature windows are significantly wider, which expand to 80−90 °C over Au/F-(1) and to 70−90 °C over the catalysts with higher F contents (Au/F-(2), Au/F-(3) and Au/F-(4)).

The stability tests carried out at 80 °C, in the presence of 15 % H_2O and 20 % CO_2, confirm the significant improvement of the activity over the F-modified samples compared with the unpromoted sample. Especially, they reveal extraordinary performance, in terms of activity and stability, of the Au/F-(1) and Au/F-(2) catalysts (Fig. 10). Over the latter, there is no trace of carbon monoxide in the reactor outlet stream. However, the catalysts with higher F loadings (Au/F-(3) and Au/F-(4)) nearly meet the target, showing a X_{CO} value of 98 %. Furthermore, over the most active catalysts, relatively high selectivity values (62 %, for Au/F-(1), and 55 %, for Au/F-(2)) are maintained up to 70 h TOS. According to XRD and BET data (not shown), no significant changes could

Table 4
Kinetic data, estimated at 80 °C, over the reduced Au/F-(x) catalysts in COTOX, COPROX and H_2 oxidation reaction, respectively.

Catalyst	COTOX[a]		COPROX[b]	H_2 oxidation[c]
	Ea, kJ mol^{-1}	r, $mmol_{CO}\ g_{Au}^{-1}\ s^{-1}$	r, $mmol_{CO}\ g_{Au}^{-1}\ s^{-1}$	r, $mmol_{H2}\ g_{Au}^{-1}\ s^{-1}$
Au/F-(0)	22.5	0.60	2.45 (100)[d]	2.15
Au/F-(1)	22.0	0.60	3.26 (100)	2.70
Au/F-(2)	26.9	0.88	3.70 (91)	2.91
Au/F-(3)	28.7	1.36	4.20 (100)	2.70
Au/F-(4)	22.0	0.76	3.44 (100)	2.46

[a] Feed gas: 1% CO and 1% O_2, balanced with He.
[b] Feed gas: 2% CO, 0.4 % O_2 and 40 % H_2, balanced with He.
[c] Feed gas: 1% O_2 and 3% H_2, balanced with He.
[d] Data corresponding to the selectivity values (%).

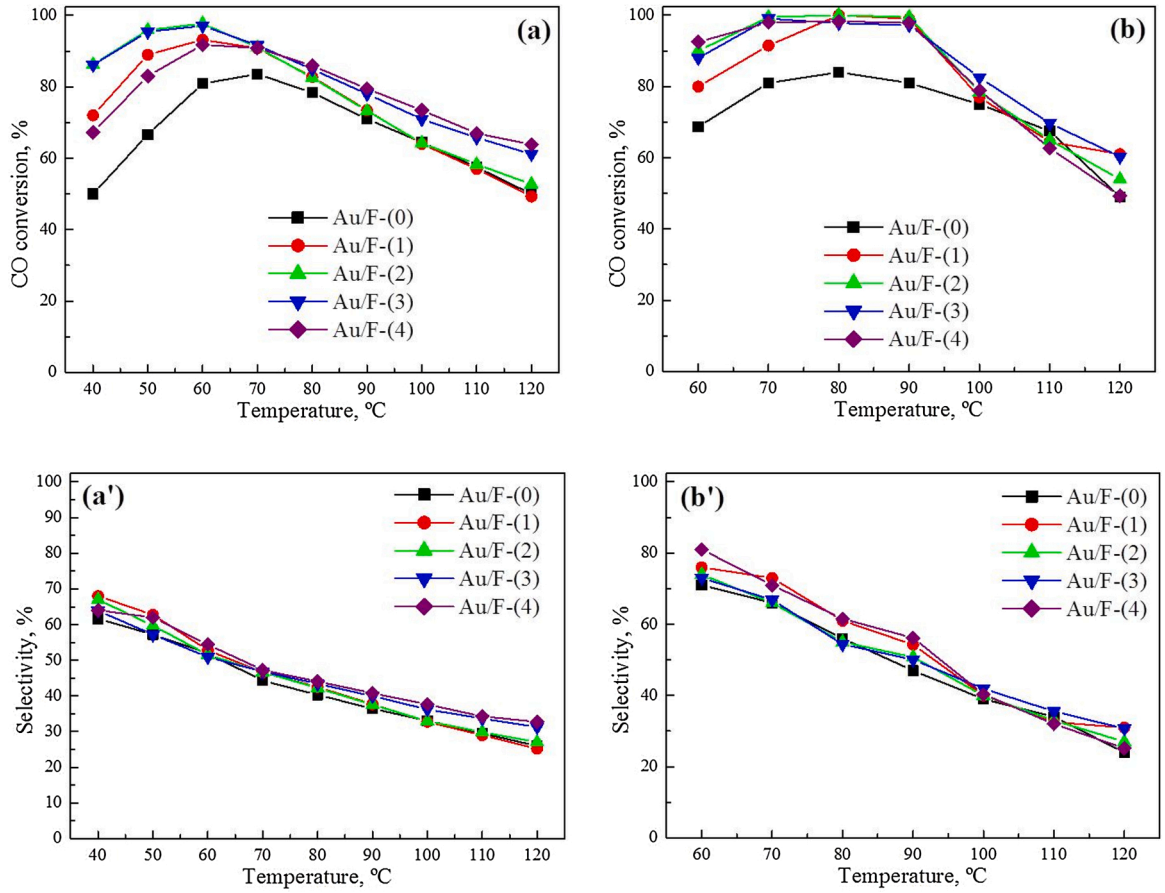

Fig. 9. Catalytic performance of the Au/F-(x) catalysts in the COPROX reaction. (a) and (a') are CO conversion and selectivity, respectively, under 1% CO, 1% O_2, and 50 % H_2 balanced in He. (b) and (b') are CO conversion and selectivity, respectively, under 1% CO, 1% O_2, 15 % H_2O, 20 % CO_2 and 50 % H_2 balanced in He (WHSV = 60,000 $cm^3\ g^{-1}$).

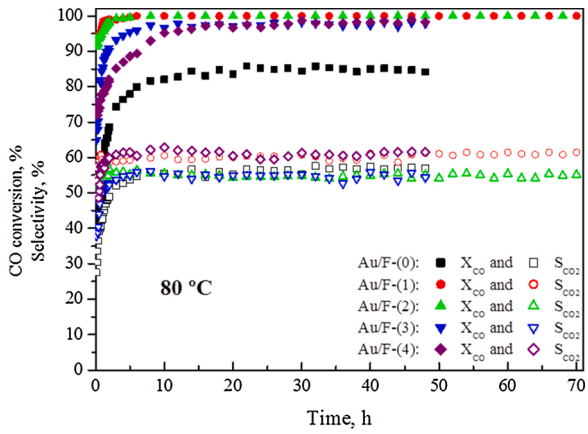

Fig. 10. Stability tests of the reduced Au/F-(x) catalysts in the COPROX reaction at 80 °C under 1% CO, 1% O_2, 15 % H_2O, 20 % CO_2 and 50 % H_2 balanced in He (WHSV = 60,000 $cm^3\ g^{-1}$).

be observed in the structural and textural properties of the spent catalysts in respect of the freshly reduced ones, which explain their high stability. Additional experiments evidence that all investigated catalysts are not active in the WGS reaction at 80 °C (not shown). Consistent with the mechanistic role of water as a co-catalyst for CO oxidation [43], the high selectivity of the Au/F-(1) catalyst compared with that of Au/F-(2) can be attributed to their distinct interaction with water molecules. It should be noted that, the former presents high capacity to chemisorb water compared with the latter (Fig. 6b). On the other hand, as reported in Table 4, the estimation of the COPROX reaction rates show that, unlike Au/F-(1), it is hard to totally suppress the H_2 oxidation reaction over the Au/F-(2) catalyst (showing a selectivity of 91 %). In consistency with this observation, the Au/F-(2) sample is intrinsically more active for H_2 oxidation (2.91 $mmol_{H2}\ g_{Au}^{-1}\ s^{-1}$) than Au/F-(1) sample (2.7 $mmol_{H2}\ g_{Au}^{-1}\ s^{-1}$). In addition, our FTIR studies of CO oxidation showed that the Au/F-(2) sample bears additional CO adsorption sites more positively charged compared with those exposed on the Au/F-(1) catalyst. Accordingly, we speculate that these additional sites are probably more active for H_2 oxidation.

On the other hand, it seems that obtaining the smallest Au nanoparticle (NP) is not a determining parameter that positively affect the performance of our Au/F-(x) catalysts; since the most active ones (Au/F-(1) and Au/F-(2)) comprise relatively larger Au particles (3.3 and 4.2 nm, respectively). This observation does agree with previous studies by Landon [2] and Shodiya [45] on the activity of highly active Au/Fe_2O_3 catalysts in the COPROX reaction. In fact, the former reported an average Au NP size around 6.7 nm and the latter observed relatively larger sizes (15−25 nm). They stressed that the CO conversion dependence on the gold NP size becomes secondary when it is supported on porous materials exhibiting suitable properties. In this sense, it seems that the inclusion of fluoride species into the apatite structure confers to the studied catalysts suitable properties giving a much more improved performance in the COPROX reaction. Our chemisorption studies, discussed above, showed a decrease in the number of basic sites with the progressive increase in the F content. Also, with reference to Au/F-(0) and Au/F-(4) samples, the partially fluoridated samples presented a lower crystallinity degree, a lower OSC activity, a larger density of the

acid sites and improved textural properties. Besides its effect on the increase of the number of acid centers, previous reports demonstrated that the incorporation of F^- into the one-dimensional OH^- chain of the HAP lattice leads to a significant increase in the proton conductivity of the material. For instance, El Hammari et al. [50] found that the fluoridation of HAP increased its conductivity by two orders of magnitude (from 5.03 10^{-5} to 7.4 10^{-7} S cm^{-1}), using 2.8 wt.% F. This change in the conduction properties of the HAP is probably one of the possible factors responsible for the significant improvement in the COPROX activity of the investigated materials. According to Saavedra et al. [51] this parameter is extremely important allowing the effective participation of water molecules in the CO oxidation mechanism. In this sense, they reported that proton transfer at the metal-support interface facilitates O_2 binding and then its activation to form Au−OOH species which reacts with adsorbed CO to form Au−COOH. In turn, the decomposition of the latter was suggested to be the rate determining step involving proton transfer to water. Considering the improvement of the proton conductivity of the HAP through the incorporation of the fluoride ions, this mechanism pathway seems to be the most prevalent one to explain the high efficiency observed on our F-modified samples.

In order to provide insight into the importance of our discovery we compare in Table 5 the performance of our catalysts with those shown over different gold catalyst formulations reported in the literature [2,3,11,12,45,48,49]. It should be highlighted that the activity of our optimized catalysts clearly outperforms state-of-the-art gold catalysts. Only two previous reports pointed out the stable and quasi-total elimination of CO ($X_{CO} \geq 99.5$ % and $S_{CO2} = 51$ %) at 80 °C, in the presence of 4.7 % H_2O and 24 % CO_2, over a 5%Au/Fe_2O_3 catalyst [2,11]. Nevertheless, our formulations are still much more efficient since their stability tests were performed at lower WHSV (12,000 mL g^{-1} h^{-1} vs. 60,000 mL g^{-1} h^{-1} used by us) and using Au loading (5 wt.%) 4.5 times higher than the one used by us (1.1 wt.%). It is also worth noting that the concentration of the added water (4.7 %) used by Landon et al. [2,11] was not sufficient to approximate the operation conditions of their Au catalysts to those required by PEMFCs. Excellent stability was also reported by Shodiya et al. [45] over an improved Au/Fe_2O_3 catalyst, but with a lower H_2O concentration (3%). In this sense, given its extraordinary performance under the most extreme conditions the Au/F-(1) sample can be considered as the most suitable catalyst for feeding PEMFC with CO-free hydrogen stream.

Considering the promising performance of the Au/F-(1) catalyst, additional experiments were carried out to study the effect of the addition of H_2O and CO_2, respectively, on its COPROX activity (Fig. 11). For the sake of comparison, the behavior of the unsubstituted sample (Au/F-(0)) was also investigated. The description of the changes observed in the performance of the two catalysts is made taking the ideal COPROX activity as a reference. Irrespective of the reaction mixture composition, the Au/F-(1) exhibits higher activity and selectivity than

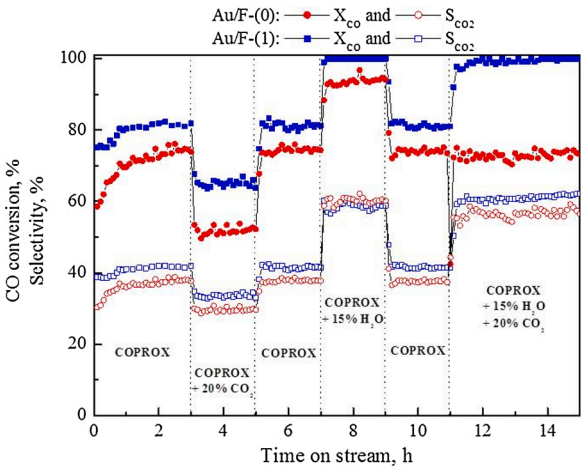

Fig. 11. Effect of H_2O and CO_2 addition on the catalytic performance of the Au/F-(0) and Au/F-(1) samples, respectively, in the COPROX reaction. The standard COPROX mixture is composed of 1% CO, 1% O_2 and 50 % H_2 balanced in He (WHSV = 60,000 cm^3 g^{-1}).

the Au/F-(0) catalyst. In the absence of water, the addition of CO_2 to the COPROX reaction mixture provokes a significant decay in the activity of the two samples. This behavior can be associated with the accumulation of carbonate [3,43]. It should be outlined that the extent of the deactivation of the unsubstituted catalyst is more profound (activity loss of 30.7 %) than that observed in the case of the Au/F-(1) catalyst (19.7 %). Interestingly, when removing CO_2, the catalysts tend to rapidly recover their COPROX activity; suggesting that the deactivation caused by the CO_2 addition is rather a reversible process. However, over the two tested catalysts, the positive effect of water addition on the COPROX activity and selectivity can be observed. According to previous studies, the presence of water helps in the decomposition of the carbonates which poison CO oxidation and in blocking H_2 adsorption sites [43,51,52]. Upon feeding water and CO_2, the behavior of the two catalysts appears to proceed via different pathways. The unsubstituted sample seems to keep its COPROX activity intact, whereas a significant increase in the S_{CO2} values can be observed. However, over the fluoridated sample there is a marked improvement in the activity and selectivity. We can conclude that, under realistic COPROX conditions (in the presence of H_2O and CO_2), the presence of water increases the selectivity of the two catalysts by decreasing the number of the H_2 oxidation reaction active sites. In parallel, it seems that the effect of water in increasing the CO oxidation active sites is only favored on the fluoridated sample. As already commented on, it seems that the improved conductivity of the fluoridated support plays a key role allowing the effective participation of water molecules in the CO oxidation mechanism through increasing

Table 5
Comparison of the catalytic performance of Au/F-(x) catalysts in realistic COPROX reaction with different gold catalyst formulations reported in the literature.

Catalyst	Au, wt.%	Feed gas composition, %					WHSV, cm^3 g^{-1} h^{-1}	T, °C	X_{CO}, %	S_{CO2}, %	TOS, h	Ref.
		CO	O_2	H_2	CO_2	H_2O						
Au/F-(0)	1.09	1	1	50	20	15	60,000	80	84	57	48	
Au/F-(1)	1.08	1	1	50	20	15	60,000	80	100	62	70	
Au/F-(2)	1.10	1	1	50	20	15	60,000	80	100	55	70	This work
Au/F-(3)	1.10	1	1	50	20	15	60,000	80	98	54	48	
Au/F-(4)	1.10	1	1	50	20	15	60,000	80	98	61	48	
Au/Fe_2O_3	5	0.9	0.9	50	22	4.7	12,000	80	99.5	51	14	[2,11]
Au/Fe_2O_3	3.3	1.03	1.37	70.1	24	3	n. d.	80	100	n. d.	200	[45]
3Au/MnAl	3.1	1	1	40	20	10	40,000	80	95	55	40	[48]
Au/La-Al_2O_3	0.82	1	1	40	20	10	60,000	80	62	n. d.	20	[3]
Au/Fe_2O_3	4.4	1	1	40	20	10	60,000	80	47	n. d.	20	[3]
Au/CeO_2 *	0.05	1	1	40	20	10	50,000	80	20	n. d.	50	[12]
1%Au/CeO_2	1	1	1	40	2	2.6	30,000	80	92	62	50	[49]

* Au single atoms.

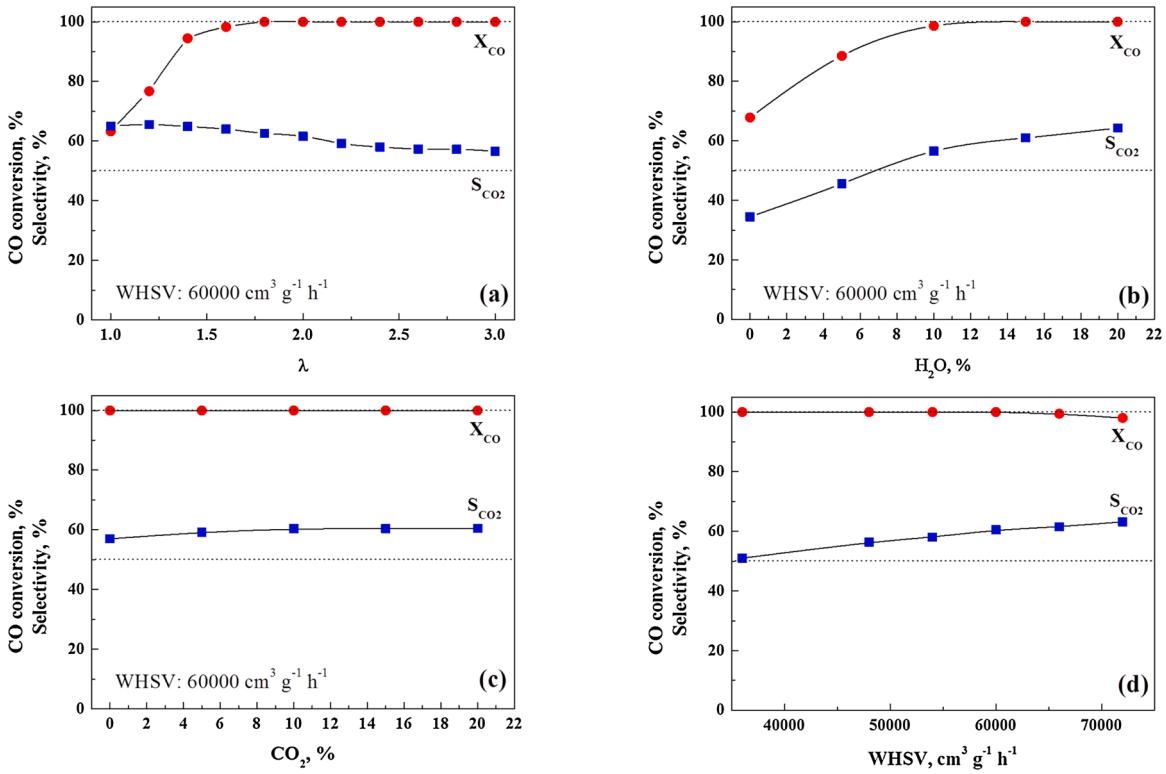

Fig. 12. Variation of the catalytic properties of Au/F-(1) sample in the COPROX reaction (at 80 °C) with (a) λ (1% CO, 1-3% O_2, 15 % H_2O, 20 % CO_2 and 50 % H_2), (b) H_2O (1% CO, 1% O_2, 0-20 % H_2O, 20 % CO_2 and 50 % H_2), (c) CO_2 (1% CO, 1% O_2, 15 % H_2O, 0-20 % CO_2 and 50 % H_2) and (d) WHSV (1% CO, 1% O_2, 15 % H_2O, 20 % CO_2 and 50 % H_2).

the number of the available active sites.

Fig. 12 reports the effect of the variation of the O_2, H_2O and CO_2 concentrations and WHSV on the catalytic properties of the Au/F-(1) sample (Fig. 12a–d, respectively). As it can be deduced from Fig. 12a, a progressive increase in the oxygen excess results in an increase in CO conversion at the expense of the CO_2 selectivity, suggesting an increase in the activity for both CO and hydrogen oxidation [46]. Thus, the total elimination of CO can be achieved under a reaction composition presenting λ values higher than 1.6. It is important to stress that over the whole investigated oxygen excess range ($1 \leq \lambda \leq 3$), the selectivity maintains acceptable values (> 56 %). Fig. 12b shows that both X_{CO} and S_{CO2} increase with increasing the concentration of H_2O, which confirms once again the positive effect of water on the CO oxidation activity. By contrast, in the presence of 20 % H_2O, no significant effect of CO_2 concentration on the activity and selectivity can be observed (Fig. 12c). On the other hand, the study of the effect of increasing WHSV, from 36,000 to 72,000 cm^3 g^{-1} h^{-1}, reveals that the catalyst maintains its capacity to completely eliminate carbon monoxide in the WHSV range of 36000−60000 cm^3 g^{-1} h^{-1} (Fig. 12d). At higher WHSV values, a smooth decrease in the X_{CO} values can be observed due to a decrease in the contact time. Nevertheless, over the whole investigated range the selectivity significantly increases with the progressive increase of space velocity.

4. Conclusions

We have designed a new catalyst formulation consisting of gold supported on fluorine-substituted HAP for the COPROX reaction. When reduced at 400 °C, these catalysts comprise relatively small Au particle sizes (< 5 nm). The partial fluoridation of HAP strongly modifies the structural, textural and chemical properties of the catalysts. This induces principally (i) a decrease in the support particle size which improves the textural properties, (ii) an increase in the surface acidity and the proton conductivity and (iii) a loss in the surface basic centers. Moreover, the FTIR studies evidence the effect of the support modification with fluorine on the electronic properties of the Au particles and the nature of the adsorption sites involved in the CO oxidation reaction.

Irrespective of the F content added, the COPROX activity is dramatically improved when compared with the free-fluorine sample. For instance, in the presence of H_2O and CO_2, unlike the Au/F-(0), over the F-modified catalysts the maximal CO conversion approaches 100 % and their temperature windows are significantly wider, which expand to 80−90 °C over Au/F-(1) and to 70−90 °C over the catalysts with higher F contents (Au/F-(2), Au/F-(3) and Au/F-(4)). The modification of the nature of the Au-support interface by inclusion of fluoride ions, providing higher conduction properties, seems to be beneficial, leading to the improvement observed.

The long-term stability tests performed at 80 °C showed that the catalyst presenting a F-substitution degree close to 29 % (Au/F-(1)) proves to be highly active (X_{CO} = 100 %), selective (S_{CO2} = 62 %) and very resistant to deactivation, even in the presence of H_2O (15 %) and CO_2 (20 %), at relatively high space velocity (60,000 cm^3 g^{-1} h^{-1}). Though the total elimination of CO is still guaranteed, an increase in the substitution degree up to 64 % decreases the selectivity to 55 %. The relatively high selectivity observed over the Au/F-(1) catalyst was linked to its (i) high capacity to chemisorb water, (ii) smaller Au particle sizes and (iii) suitable electronic properties of Au under the reaction mixtures.

It should be highlighted that the activity of our optimized sample clearly outperforms state-of-the-art gold catalysts. These unprecedented performances introduce the Au/F(x)-HAP catalysts as a viable solution for an effective elimination of CO to feed PEMFCs with CO-free hydrogen streams.

Work is in progress in order to achieve further improvements in this new class of active catalysts.

CRediT authorship contribution statement

Zouhair Boukha: Conceptualization, Investigation, Methodology, Software, Data curation, Writing and Original draft preparation, Funding acquisition. **Juan R. González-Velasco:** Conceptualization, Reviewing, Funding acquisition. **Miguel A. Gutiérrez-Ortiz:** Conceptualization, Reviewing, Funding acquisition.

Declaration of Competing Interest

The authors report no declarations of interest.

Acknowledgments

The financial support for this work provided by Ministerio de Economía y Competitividad (CTQ2015-73219-JIN (AEI/FEDER/UE) and ENE2016-74850-R) and Basque Government (GIC IT-1297-19) is gratefully acknowledged. Likewise, the technical support provided by SGIker (UPV/EHU) is gratefully acknowledged.

Appendix A. Supplementary data

Supplementary material related to this article can be found, in the online version, at doi:https://doi.org/10.1016/j.apcatb.2021.120142.

References

[1] D.L. Trimm, Z.I. Önsan, Onboard fuel conversion for hydrogen-fuel-cell-driven vehicles, Catal. Rev. Sci. Eng. 43 (2001) 31.
[2] P. Landon, J. Ferguson, B.E. Solsona, T. Garcia, S. Al-Sayari, A.F. Carley, A. A. Herzing, C.J. Kiely, M. Makkee, J.A. Moulijn, A. Overweg, S.E. Golunski, G. J. Hutchings, Selective oxidation of CO in the presence of H_2, H_2O and CO_2 utilising Au/α-Fe_2O_3 catalysts for use in fuel cells, J. Mater. Chem. 16 (2006) 199–208.
[3] Q. Lin, B. Qiao, Y. Huang, L. Li, J. Lin, X.Y. Liu, A. Wang, W.-C. Li, T. Zhang, La-doped Al_2O_3 supported Au nanoparticles: highly active and selective catalysts for PROX under PEMFC operation conditions, Chem. Commun. 50 (2014) 2721–2724.
[4] M.M. Schubert, A. Venugopal, M.J. Kahlich, V. Plzak, R.J. Behm, Influence of H_2O and CO_2 on the selective CO oxidation in H_2-rich gases over Au/α-Fe_2O_3, J. Catal. 222 (2004) 32–40.
[5] O.H. Laguna, W.Y. Hernandez, G. Arzamendi, L.M. Gandía, M.A. Centeno, J. A. Odriozola, Gold supported on CuO_x/CeO_2 catalyst for the purification of hydrogen by the CO preferential oxidation reaction (PROX), Fuel 118 (2014) 176–185.
[6] P. Lakshmanan, E.D. Park, Preferential CO oxidation in H_2 over Au/La_2O_3/Al_2O_3 catalysts: the effect of the catalyst reduction method, Catalysts 8 (5) (2018) 183.
[7] K. Liu, A. Wang, T. Zhang, Recent advances in preferential oxidation of CO reaction over platinum group metal catalysts, ACS Catal. 2 (2012) 1165–1178.
[8] P. Jing, X. Gong, B. Liu, J. Zhang, Recent advances in synergistic effect promoted catalysts for preferential oxidation of carbon monoxide, Catal. Sci. Technol. 10 (2020) 919–934.
[9] T. Tabakova, F. Boccuzzi, M. Manzoli, D. Andreeva, FTIR study of low-temperature water-gas shift reaction on gold/ceria catalyst, Appl. Catal. A-Gen. 252 (2003) 38–397.
[10] P. Naknam, A. Luengnaruemitchai, S. Wongkasemjit, S. Osuwan, Preferential catalytic oxidation of carbon monoxide in presence of hydrogen over bimetallic AuPt supported on zeolite catalysts, J. Power Sci. 165 (2007) 353–358.
[11] P. Landon, J. Ferguson, B.E. Solsona, T. Garcia, A.F. Carley, A.A. Herzing, C. J. Kiely, S.E. Golunski, G.J. Hutchings, Selective oxidation of CO in the presence of H_2, H_2O and CO_2 via gold for use in fuel cells, Chem. Commun. (27) (2005) 3385–3387.
[12] B. Qiao, J. Liu, Y.G. Wang, Q. Lin, X. Liu, A. Wang, J. Li, T. Zhang, J. Liu, Highly efficient catalysis of preferential oxidation of CO in H2-Rich stream by gold single-atom catalysts, ACS Catal. 5 (2015) 6249–6254.
[13] Y.-X. Miao, L. Shi, Q. Sun, W.-C. Li, A highly efficient potassium-treated Au-Cu/Al_2O_3 catalyst for the preferential oxidation of carbon monoxide, RSC Adv. 6 (2016) 24603–24609.
[14] P. Lakshmanan, J.E. Park, B. Kim, E.D. Park, Preferential oxidation of CO in a hydrogen-rich stream over Au/MO_x/Al_2O_3 (M = La, Ce, and Mg) catalysts, Catal. Today 265 (2016) 19–26.
[15] H. Tang, J. Wei, F. Liu, B. Qiao, X. Pan, L. Li, J. Liu, J. Wang, T. Zhang, Strong metal-support interactions between gold nanoparticles and nonoxides, J. Am. Chem. Soc. 138 (2016) 56–59.
[16] Z. Boukha, A. Choya, M. Cortés-Reyes, B. de Rivas, L.J. Alemany, J.I. J.R.González-Velasco, Gutiérrez-Ortiz, R. López-Fonseca, Influence of the calcination temperature on the activity of hydroxyapatite-supported palladium catalyst in the methane oxidation reaction, Appl. Catal. B-Environ. 277 (2020), 119280.
[17] Z. Boukha, J.R. González-Velasco, M.A. Gutiérrez-Ortiz, Platinum supported on lanthana-modified hydroxyapatite samples for realistic WGS conditions: on the nature of the active species, kinetic aspects and the resistance to shut-down/start-up cycles, Appl. Catal. B-Environ. 270 (2020), 118851.
[18] Z. Boukha, M.P. Yeste, M.Á. Cauqui, J.R. González-Velasco, Influence of Ca/P ratio on the catalytic performance of Ni/hydroxyapatite samples in dry reforming of methane, Appl. Catal. A-Gen. 580 (2019) 34–45.
[19] Z. Boukha, J.L. Ayastuy, M. Cortés-Reyes, L.J. Alemany, J.R. González-Velasco, M. A. Gutiérrez-Ortiz, Catalytic performance of Cu/hydroxyapatite catalysts in CO preferential oxidation in H_2-rich stream, Int. J. Hydrogen Energy 44 (2019) 12649–12660.
[20] Z. Boukha, J.L. Ayastuy, J.R. González-Velasco, M.A. Gutiérrez-Ortiz, Water-gas shift reaction over a novel Cu-ZnO/HAP formulation: enhanced catalytic performance in mobile fuel cell applications, Appl. Catal. A-Gen. 566 (2018) 1–14.
[21] Z. Boukha, J.L. Ayastuy, J.R. González-Velasco, M.A. Gutiérrez-Ortiz, CO elimination processes over promoter-free hydroxyapatite supported palladium catalysts, Appl. Catal. B-Environ. 201 (2017) 189–201.
[22] Z. Boukha, M. Kacimi, M. Ziyad, A. Ensuque, F. Bozon-Verduraz, Comparative study of catalytic activity of Pd loaded hydroxyapatite and fluoroapatite in butan-2-ol conversion and methane oxidation, J. Mol. Catal. A-Chem. 270 (2007) 205–213.
[23] Z. Boukha, M. Kacimi, M.F.R. Pereira, J.L. Faria, J.L. Figueiredo, M. Ziyad, Methane dry reforming on Ni loaded hydroxyapatite and fluoroapatite, Appl. Catal. A-Gen. 317 (2007) 299–309.
[24] Z. Boukha, J. González-Prior, B. Rivas, J.R. González-Velasco, R. López-Fonseca, J. I. Gutiérrez-Ortiz, Synthesis, characterisation and behaviour of Co/hydroxyapatite catalysts in the oxidation of 1,2-dichloroethane, Appl. Catal. B-Environ. 190 (2016) 125–136.
[25] Y. Sa, Y. Guo, X. Feng, M. Wang, P. Li, Y. Gao, X. Yang, T. Jiang, Are different crystallinity-index-calculating methods of hydroxyapatite efficient and consistent? New J. Chem. 41 (2017) 5723.
[26] T. Nakano, A. Tokumura, Y. Umakoshi, Variation in crystallinity of hydroxyapatite and the related calcium phosphates by mechanical grinding and subsequent heat treatment, Metall. Mater. Trans. A. 33A (2002) 251.
[27] L.M. Rodríguez-Lorenzo, J.N. Hart, K.A. Gross, Influence of fluorine in the synthesis of apatites. Synthesis of solid solutions of hydroxy-fluorapatite, Biomaterials 24 (2003) 3777–3785.
[28] K. Pajor, L. Pajchel, J. Kolmas, Hydroxyapatite and fluorapatite in conservative dentistry and oral implantology-a review, Materials 12 (2019) 2683.
[29] C. You, S. Kim, M. Ahn, S. Kim, S. Kim, Evaluation of hydroxyl groups on hydroxyapatite and calcium metaphosphate by grafting TEOS and APTES, Key Eng. Mat. 342-343 (2007) 677–680.
[30] T. Schalow, M. Laurin, B. Brandt, S. Schauermann, S. Guimond, H. Kuhlenbeck, D. E. Starr, S.K. Shaikhutdinov, J. Libuda, H.- Freund, Oxygen storage at the metal/oxide interface of catalyst nanoparticles, Angew. Chem. Int. Ed. 44 (2005) 7601–7605.
[31] E. Ozkan, P. Cop, F. Benfer, A. Hofmann, M. Votsmeier, J.M. Guerra, M. Giar, C. Heiliger, H. Over, B.M. Smarsly, Rational synthesis concept for cerium oxide nanoparticles: on the impact of particle size on the oxygen storage, J. Phys. Chem. C 124 (2020) 8736–8748.
[32] X. Liu, M.- Liu, Y.- Luo, C.- Mou, S.D. Lin, H. Cheng, J.- Chen, J.- Lee, T.- Lin, Strong metal-support interactions between gold nanoparticles and ZnO nanorods in CO oxidation, J. Am. Chem. Soc. 134 (2012) 10251–10258.
[33] F. Boccuzzi, A. Chiorino, M. Manzoli, D. Andreeva, T. Tabakova, FTIR study of the low-temperature water-gas shift reaction on Au/Fe_2O_3 and Au/TiO_2 catalysts, J. Catal. 188 (1999) 176–185.
[34] M. Li, Z. Wu, S.H. Overbury, CO oxidation on phosphate-supported Au catalysts: effect of support reducibility on surface reactions, J. Catal. 278 (2011) 133–142.
[35] T. Venkov, H. Klimev, M.A. Centeno, J.A. Odriozola, K. Hadjiivanov, State of gold on an Au/Al_2O_3 catalyst subjected to different pre-treatments: an FTIR study, Catal. Commun. 7 (2006) 308–313.
[36] J.- Grunwaldt, A. Baiker, Gold/titania interfaces and their role in carbon monoxide oxidation, J. Phys. Chem. B 103 (1999) 1002–1012.
[37] G. Che-Galicia, V. Ruíz-Santoyo, R. Zanella, N.Y. Mendoza-González, I.I. Ruiz-López, A. Sampieri, Kinetic mechanism of CO oxidation on gold catalyst supported on TiSBA-15 previously treated in a hydrogen atmosphere, Chem. Eng. J. 405 (2021), 126644.
[38] W. Deng, C. Carpenter, N. Yi, M. Flytzani-Stephanopoulos, Comparison of the activity of Au/CeO_2 and Au/Fe_2O_3 catalysts for the CO oxidation and the water-gas shift reactions, Top. Catal. 44 (2007) 199–208.
[39] M. Daté, M. Okumura, S. Tsubota, M. Haruta, Vital role of moisture in the catalytic activity of supported gold nanoparticles, Angew. Chem. Int. Ed. 43 (2004) 2129–2132.
[40] J.T. Calla, M.T. Bore, A.K. Dayte, R.J. Davis, Effect of alumina and titania on the oxidation of CO over Au nanoparticles evaluated by 13C isotopic transient analysis, J. Catal. 238 (2006) 458–467.
[41] M.M. Schubert, S. Hackenberg, A.C. van Veen, M. Muhler, V. Plzak, R.J. Behm, CO oxidation over supported gold catalysts -"Inert" and "active" support materials and their role for the oxygen supply during reaction, J. Catal. 197 (2001) 113–122.
[42] J. Huang, L. Wang, Y. Liu, Y. Cao, H. He, K. Fan, Gold nanoparticles supported on hydroxylapatite as high-performance catalysts for low temperature CO oxidation, Appl. Catal. B-Environ. 101 (2011) 560–569.
[43] J. Saavedra, T. Whittaker, Z. Chen, C.J. Pursell, R.M. Rioux, B.D. Chandler, Controlling activity and selectivity using water in the Au-catalysed preferential oxidation of CO in H_2, Nat. Chem. 8 (2016) 584–589.
[44] E. Quinet, F. Morfin, F. Diehl, P. Avenier, V. Caps, J. Roussel, Hydrogen effect on the preferential oxidation of carbon monoxide over alumina-supported gold nanoparticles, Appl. Catal. B-Environ. 80 (2008) 195–201.

[45] T. Shodiya, O. Schmidt, W. Peng, N. Hotz, Novel nano- scale Au/α-Fe2O3 catalyst for the preferential oxidation of CO in biofuel reformate gas, J. Catal. 300 (2013) 63–69.
[46] T.R. Reina, E. Papadopoulou, S. Palma, M.A. Centeno, T. Ioannides, J.A. Odriozola, Could an efficient WGS catalyst be useful in the CO-PrOx reaction? Appl. Catal. B-Environ. 150-151 (2014) 554–563.
[47] L.C. Grabow, A.A. Gokhale, S. Evans, J.A. Domesic, M.J. Mavrikakis, Mechanism of the water gas shift reaction on Pt: first principles, experiments, and microkinetic modeling, J. Phys. Chem. C. 112 (2008) 4608–4617.
[48] Y.- Miao, W.- Li, Q. Sun, L. Shi, L. He, J. Wang, G.- Deng, A.- Lu, Nanogold supported on manganese oxide doped alumina microspheres as a highly active and selective catalyst for CO oxidation in a H_2-rich stream, Chem. Commun. 51 (2015) 17728–17731.
[49] A. Luengnaruemitchai, S. Osuwan, E. Gulari, Selective catalytic oxidation of CO in the presence of H_2 over gold catalyst, Int. J. Hydrogen Energy 29 (2004) 429–435.
[50] L.E.L. Hammari, A. Laghzizil, P. Barboux, A. Saoiabi, K. Lahlil, Crystallinity and fluorine substitution effects on the proton conductivity of porous hydroxyapatites, J. Solid State Chem. 177 (2004) 134–138.
[51] J. Saavedra, H.A. Doan, C.J. Pursell, L.C. Grabow, B.D. Chandler, The critical role of water at the gold-titania interface in catalytic CO oxidation, Science 345 (2014) 1599–1602.
[52] B. Schumacher, Y. Denkwitz, V. Plzak, M. Kinne, R.J. Behm, Kinetics, mechanism, and the influence of H_2 on the CO oxidation reaction on a Au/TiO_2 catalyst, J. Catal. 224 (2004) 449–462.